

Kenneth Clark

Department of Mechanical
and Nuclear Engineering,
The Pennsylvania State University,
University Park, PA 16802
e-mail: kpc139@psu.edu

Michael Barringer

Department of Mechanical
and Nuclear Engineering,
The Pennsylvania State University,
University Park, PA 16802
e-mail: mbarringer@psu.edu

Karen Thole

Department of Mechanical
and Nuclear Engineering,
The Pennsylvania State University,
University Park, PA 16802
e-mail: kthole@engr.psu.edu

Carey Clum

Pratt & Whitney,
East Hartford, CT 06118
e-mail: carey.clum@pw.utc.com

Paul Hiester

Pratt & Whitney,
East Hartford, CT 06118
e-mail: paul.hiester@pw.utc.com

Curtis Memory

Pratt & Whitney,
East Hartford, CT 06118
e-mail: curtis.memory@pw.utc.com

Christopher Robak

Pratt & Whitney,
East Hartford, CT 06118
e-mail: christopher.robak@pw.utc.com

Effects of Purge Jet Momentum on Sealing Effectiveness

Driven by the need for higher cycle efficiencies, overall pressure ratios for gas turbine engines continue to be pushed higher thereby resulting in increasing gas temperatures. Secondary air, bled from the compressor, is used to cool turbine components and seal the cavities between stages from the hot main gas path. This paper compares a range of purge flows and two different purge hole configurations for introducing the purge flow into the rim cavities. In addition, the mate face gap leakage between vanes is investigated. For this particular study, stationary vanes at engine-relevant Mach and Reynolds numbers were used with a static rim seal and rim cavity to remove rotational effects and isolate gas path effects. Sealing effectiveness measurements, deduced from the use of CO₂ as a flow tracer, indicate that the effectiveness levels on the stator and rotor side of the cavity depend on the mass and momentum flux ratios of the purge jets relative to the swirl velocity. For a given purge flow rate, fewer purge holes resulted in better sealing than the case with a larger number of holes. [DOI: 10.1115/1.4034545]

Introduction

Gas turbines are used extensively in both aviation propulsion and power generation applications, so increases in efficiency are desirable. To increase cycle efficiency, overall pressure ratios for gas turbine engines continue to rise causing increased turbine inlet temperatures, which can lead to component durability concerns and increased maintenance costs. Secondary air, which is bled from the compressor, is required to both cool components and seal cavities against hot gas ingestion. Efficient use of the secondary air is necessary as excessive use causes a parasitic loss in engine efficiency.

The cooling air is directed to the cavity regions inboard of the airfoil platform to counter the effects of hot gas ingestion, which is driven by pressure fields in the main gas path, disk pumping in the cavities, and turbulent transport between the gas path and cavities. Rim seals located at the airfoil endwall platform between rotating and stationary components are used to isolate the main gas path from the cavities, minimize ingestion, and maintain

component durability. Rim seals use combinations of radial and axial overlapping geometries to minimize hot gas ingestion. Sealing air is still required to purge ingested hot gas from the cavity. Additionally, gaps between segmented hardware of a single stage and secondary air leakages through those gaps contribute to the already complex flow patterns in the rim seal and cavity regions. Because of this geometric and flow field complexity, there is a need for high fidelity predictive methods to accurately model the cavity flow physics. Experiments at engine-relevant conditions are required to validate new designs and computational tools.

This paper provides a unique study as the seal and cavity geometry is engine-relevant unlike many past studies that have used simplified geometries, and the purge flow delivery methods are investigated. The combination of these two factors has not been previously reported. This paper describes the sealing effectiveness for a range of different flow conditions and sealing configurations for an engine-realistic rim seal for engine-relevant Mach and Reynolds numbers without rotational effects. The use of CO₂ as a tracer gas in the secondary air was used to quantify sealing effectiveness throughout the rim seal and rim cavity. For this study, sealing effectiveness measurements were made only for the first vane with a static rim seal and rim cavity in place of the 1.5-stage test turbine.

Contributed by the Heat Transfer Committee of ASME for publication in the JOURNAL OF ENGINEERING FOR GAS TURBINES AND POWER. Manuscript received July 6, 2016; final manuscript received July 22, 2016; published online October 4, 2016. Editor: David Wisler.

Review of Literature

Many rim seal and hot gas ingestion studies exist in the open literature, but there are few with engine-relevant geometries found in modern turbines. Several studies have identified the effectiveness of radial overlap seals and double seals [1–3]. Others have identified the importance of rotational effects, such as disk pumping [3–5]. Additional factors such as three-dimensional, unsteady interactions of the vane–blade pressure fields have been shown to affect ingestion into the rim seal region [6]. Rim seal geometries in turbine engines are designed to minimize ingestion of hot main gas path flow into regions under the airfoil platforms. The majority of the rim seal studies in the literature, however, have used simplified geometries and provided important fundamental knowledge of cavity flows, rim seals, and hot gas ingestion. Although some engine-realistic rim seals have been published [7–10], there is a need for more studies in the open literature that include the complex overlaps, buffer cavities, and flow physics of engine-realistic rim seals.

In addition to complex rim seal geometries, the effects of the methods used to deliver the purge flow are not well understood. The different methods for delivering purge flow to the rim cavity have not been studied extensively, but have been shown to affect the level of ingestion in a few papers. Purge flow angling and purge flow momentum have been found to affect cavity sealing effectiveness. Measurements by Coren et al. [11] indicated that the cavity sealing effectiveness varied greatly with the number of purge flow jets entering a blade–vane cavity. As the number of purge holes decreased, jet momentum increased and the purge flow spread throughout the rim cavity leading to more effective rotor disk cooling. A companion computational fluid dynamics (CFD) study by Andreini et al. [12] showed that the cavity flow dynamics differed with purge air delivery angles and purge hole locations. Both the axial and tangential purge flow momentum was shown to affect the cavity sealing effectiveness. As the purge holes angled toward the rotor, the disk experienced more effective cooling for both low and high purge flow rates. For tangentially angled purge holes, the flow provided significant stator side cooling. Measurements by Coren et al. [11] also supported these findings.

To accurately represent the flow physics driving hot gas ingestion, it is important that experiments are performed at engine-relevant conditions. In addition to rotational Reynolds number [3–5], the Mach number at the upstream airfoil exit has been shown to be important in accurately predicting ingestion. Using simplified but relevant axial and radial overlap rim seals, Teuber et al. [13] showed that the minimum flow rate required to fully seal the rim cavity increased with airfoil exit Mach number. Experiments were only performed up to $Ma = 0.44$, but CFD solutions were generated up to $Ma = 0.86$ showing an increase in the vane exit nondimensional pressure difference, which has been

shown to significantly affect ingestion [4,14]. Additional experimental work at engine-relevant Mach numbers is required to fully understand sealing effectiveness at engine-relevant conditions and further validate computational models.

Gibson et al. [8] showed that the trends obtained in a low-speed linear cascade without rotational effects were applicable to rotating rim seals as long as a proper crossflow was introduced at the rim seal and trench. A sector-based annular cascade study by Bunker et al. [15] at engine-relevant Mach numbers showed that cascade measurements aid in understanding and validating key ingestion flow conditions, although rotation is required to fully represent the instantaneous and time-averaged physics.

Although the effects of rotation are important to fully represent rim cavity flows, this paper presents a fundamental study varying the purge air flow rates and delivery methods in an engine-realistic rim seal at engine-relevant Mach numbers without the effects of rotation to isolate gas path effects. In the configuration presented in this paper, the hardware permitted investigation of ingestion dynamics where the gas path contained only an upstream vane row. No rotor or rotational component was present in the rim cavity. Thus, the results are most applicable to the externally induced ingestion regime as discussed in Refs. [2] and [14], where ingestion is modeled as being driven by the pressure field in the main gas path. By isolating nonrotating effects in this study, we can determine the degree to which they contribute to hot gas ingestion. The work presented in this paper is unique given that realistic geometries are operating at or near engine-relevant conditions. Measurements included the use of a tracer gas to deduce the flow phenomena in the cavity region.

Description of Facility and Turbine

The experiments presented in this paper were performed in a steady-state, turbine research facility, the full design of which was described by Barringer et al. [16]. A detailed description of the test turbine and instrumentation used in these experiments was given by Clark et al. [17]. A brief review of the test facility, test turbine, and instrumentation will be provided in this section.

The test facility was an open-loop, steady-state, flow path capable of simulating engine-relevant conditions for realistic turbine hardware as shown in Fig. 1. The facility operating conditions are given in Table 1. A large industrial compressor provided high-pressure air through the turbine test section. A second compressor installed in parallel to the first will be used in future tests to double the mass flow rate capability. For the experiments presented in this paper, one compressor provided enough high-pressure air to the facility for half-span airfoils. Given the focus of this paper was on the sealing performance of the turbine rim seal and purge flows, it was deemed appropriate to use only half-span airfoils similar to previous researchers [2,7,18]. The turbine was designed to produce the same pressure field near the rim seal as a turbine with full span airfoils.

A portion of the compressor discharge air was also used to supply the secondary air inboard of the platform of the turbine test section. The secondary air was cooled in a heat exchanger and flowed into the test section through hoses routed through the inner diameter of the test turbine. The secondary air flows were independently controlled with the mass flow rate being measured by a turbine flow meter.

The facility included instrumentation, as shown in Fig. 1, to monitor the operating conditions. Facility temperatures, pressures, and flow rates were, respectively, measured with resistance temperature devices, pressure transducers, and calibrated venturi flow meters. Additional details regarding the facility instrumentation were given in Ref. [17]. Flow control valves and a programmable logic controller (PLC) were used to control the facility operating conditions. Emergency situations were mitigated by the PLC and fast-acting safety valves that diverted flow through the by-pass.

The design of the test turbine was a 1.5-stage (vane–blade–vane) turbine. For this paper, the test turbine included a half stage

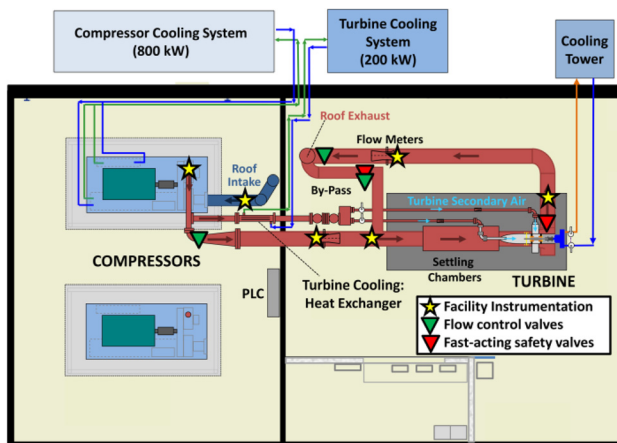


Fig. 1 START facility layout

Table 1 START facility operating conditions

Parameters	Values
Compressor discharge pressure	480 kPa
Compressor discharge temperature	395 K
Compressor mass flow rate (single)	5.7 kg/s
Vane exit Mach number	0.7
Vane exit Reynolds number ^a	6×10^5
Purge flow rate—150 holes	Up to 2.7% ^b
Purge flow rate—16 holes	Up to 0.5% ^b
Mate face gap (MFG) leakage flow rate	Up to 0.4% ^b
Purge flow rate—16 holes with mate face gap leakage flow rate	Up to 1.0% ^b

^aBased on vane exit velocity magnitude.

^bBased on full span main gas path flow rate.

(vane only) turbine with an engine-realistic rim seal and rim cavity design. A cross section of the test turbine is provided in Fig. 2 with a detailed cross section of the rim seal and rim cavity geometry given in Fig. 3. Figure 3 also provides the nomenclature that will be used to describe the turbine throughout this paper. The labeled regions delineate the areas that will be referred to as the trench, rim seal, and rim cavity.

The secondary air supply entered the test turbine and passed through successive baffle plates to ensure that uniform flow entered the first vane plenum, which in turn supplied the controlled purge and leakage flows associated with the first vane. Two different secondary flows are presented in this paper as shown in Fig. 3. The purge flow entered the rim cavity through uniformly spaced circular holes oriented in the axial direction. The leakage flow, hereafter referred to as the mate face gap leakage, was directed through slots at the interfaces between adjoining vane doublets to the rim seal. Four secondary flow configurations will be discussed in this paper: (1) the purge flow with 150 holes, (2) the purge flow with 16 holes, (3) the mate face gap (MFG) leakage flow, and (4) the purge flow with 16 holes and the mate face gap leakage flow. The ranges of flow rates for each configuration are provided in Table 1. It is important to note that the flow rates presented in this paper are normalized as a percent of the full span turbine inlet mass flow rate rather than the half-span turbine inlet mass flow rate. Although half-span airfoils were used in this study, the results were more directly comparable to operating turbines by using the full span mass flow percentages.

The test turbine was instrumented with several static pressure taps that were used for pressure and gas sampling measurements as reported by Clark et al. [17]. Figure 4 shows a cross section of the test turbine with the instrumentation. The inset image shows the circumferential arrangement. The first vanes were additively manufactured through a metal laser sintering process in pairs, or doublets, and as such, integrated static pressure taps were designed into the vanes. The static pressure taps were spread

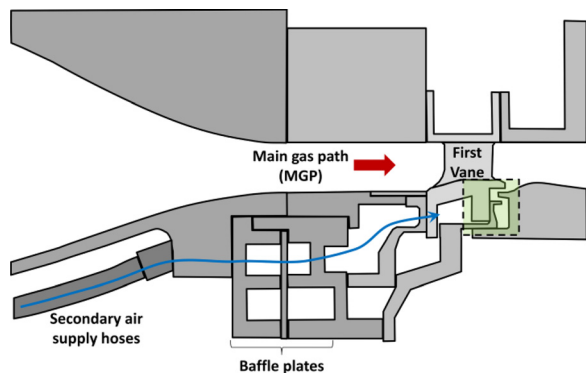


Fig. 2 Test turbine cross section

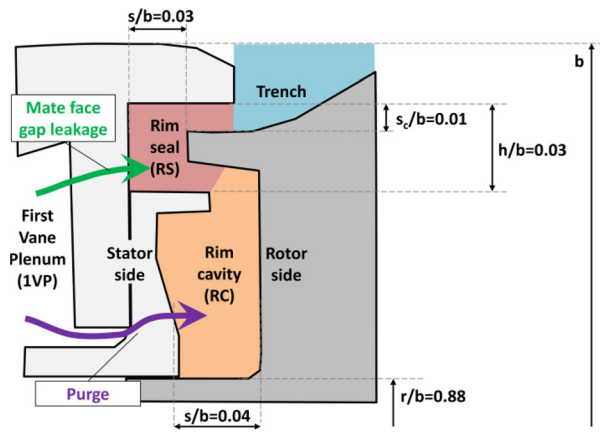


Fig. 3 Test turbine nomenclature and geometric parameter definitions

throughout the rim seal as indicated in Fig. 4. Each of these radial locations had a series of pressure taps at several circumferential locations allowing for detailed spatially resolved measurements with true scale engine hardware.

To characterize the rim seal performance and determine the flow patterns in the rim seal and rim cavity, a CO₂ tracer gas was used to measure concentration effectiveness. The definition of concentration effectiveness used in this paper is given in Eq. (1)

$$\varepsilon_c = \frac{c - c_\infty}{c_s - c_\infty} \quad (1)$$

where c is the measured CO₂ molar concentration, and the subscripts ∞ and s correspond, respectively, to the main gas path and the secondary air supply. Details regarding the CO₂ injection system, the sampling system, the gas analyzer as well as a full validation of the technique are provided in Ref. [17].

The secondary air supply was seeded with 1% CO₂ by volume. Gas samples were extracted through the sampling taps shown in Fig. 4 at a constant sampling flow rate of 2×10^{-6} kg/s, corresponding to isokinetic sampling conditions. Continuous flow was sent to a gas analyzer that measured the CO₂ molar concentration with an accuracy of $\pm 1\%$ of the full scale range, and a 60 s time-average was computed after the analyzer signal steadied with time. The overall uncertainty in the concentration effectiveness measurements was $\varepsilon_c = \pm 0.015$, and the repeatability was typically within $\varepsilon_c = \pm 0.015$.

Facility and First Vane Benchmarking

The test turbine and facility were shown to be successfully benchmarked by Clark et al. [17]. Additional benchmarking will

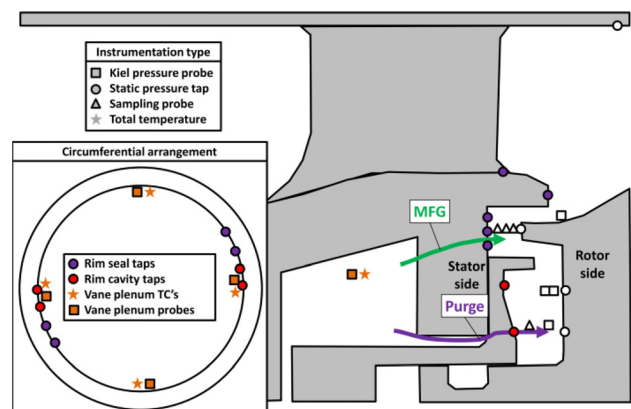


Fig. 4 Test turbine instrumentation

be provided in this section, particularly in terms of the circumferential uniformity and a comparison with CFD pretest predictions. The measurements presented in this section were obtained with the turbine vane operating at design conditions.

The vane aerodynamic loading is shown in Fig. 5 for two vanes at 50% span. The measurements on the different vanes agree within $p/p_t = \pm 0.005$ on average, which is equal to the overall uncertainty of $p/p_t = \pm 0.005$, showing that circumferential uniformity was achieved in the main gas path. Repeatability for each measurement location was previously shown to be within $p/p_t = \pm 0.002$ [17]. The vanes were fore-loaded, with a sharp acceleration evident on the first 20% wetted distance on the suction surface for all the spans. From 65% to 100% wetted distance on the suction surface, the pressure was relatively constant until downstream where the pressure and suction side pressures converged at the vane trailing edge.

Although computational simulations were not the focus of this paper, blind pretest numerical predictions were performed. The CFD loading predictions are also given in Fig. 5 and showed good agreement with the measurements in the main gas path. Good agreement was also observed in steep gradient regions such as from 10% to 40% wetted distance. Although not shown in Fig. 5, similar circumferential uniformity and agreement between CFD and the measurements were observed at 10% and 90% spans.

Many ingestion models rely on the nondimensional pressure difference, $\Delta p/p_{t,in} = (p_{max} - p_{min})/p_{t,in}$, at the rim seal as a boundary condition [2,14]. To determine the pressure boundary conditions on the rim seal, static pressures were measured on the endwall at the vane trailing edge, at the platform trailing edge (22% chord downstream of the vane trailing edge), and in the rim seal (8% chord upstream of the vane trailing edge) as shown in Fig. 6. The inset image shows the axial and radial locations of the measurements where different symbols correspond to measurements on vanes located 180 deg apart. Each of the indicated locations comprised several taps in the circumferential direction. The vane trailing edge taps were equally spaced in the passage between the vanes of the doublet, and the platform trailing edge taps were equally spaced across 1.5 vane pitches. It should be noted that the measurements shown in Fig. 6 were obtained with no purge or leakage flows. Although not shown here, no changes were observed in the vane trailing edge and platform trailing edge pressure profiles even at high purge and leakage flows; however, as expected, the pressure in the rim seal was observed to increase slightly with purge flow.

It is first noted that the measurements given in Fig. 6 showed good agreement between the measurements on different vanes indicating that circumferential uniformity was achieved in the main gas path and trench. The average difference between the measurements was $p/p_t = \pm 0.009$ at both the vane trailing edge and at the platform trailing edge. The measurements and the

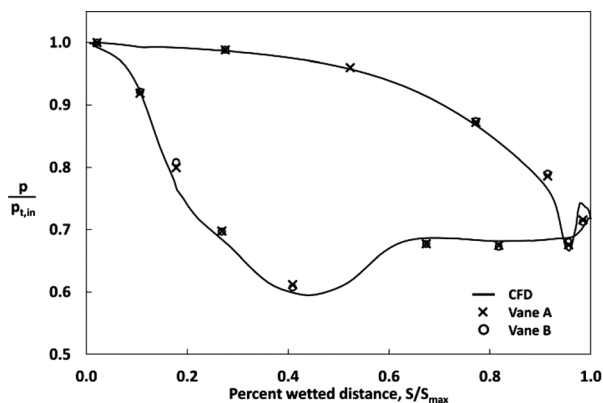


Fig. 5 First vane aerodynamic loading at 50% span compared to CFD pretest predictions

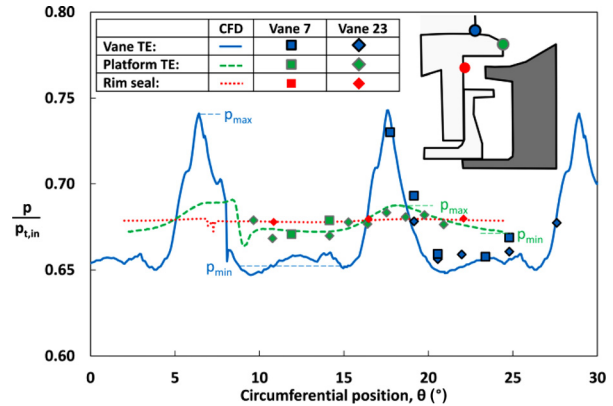


Fig. 6 Pressures on vane trailing edge, platform trailing edge (22% C_x downstream of vane trailing edge), and in rim seal (8% C_x upstream of vane trailing edge) for the no leakage case compared to CFD pretest predictions

pretest predictions agreed well with each other, including the magnitudes, widths, and locations of the pressure peaks, as shown in Fig. 6. The measurements and CFD agreed within an average difference of $p/p_t = \pm 0.004$, ± 0.001 , and ± 0.0005 at the vane trailing edge, platform trailing edge, and the rim seal, respectively. The pressure peaks due to the vane potential field can be seen at the trailing edge at $\theta = 6$ deg, 18 deg, and 29 deg.

At the platform trailing edge shown in Fig. 6, located at 22% axial chord downstream of the vane trailing edge, there was a strong mixing in the trench region and flow separation over the step that resulted in a relatively flat static pressure across the trailing edge. The nondimensional pressure difference, $\Delta p/p_{t,in} = (p_{max} - p_{min})/p_{t,in}$, at the platform trailing edge decayed to 17% of the vane trailing edge value. Full attenuation of vane exit potential field was observed in the rim seal where there was essentially no circumferential variation.

Although the rim seal and cavity were static for these particular experiments, significant tangential velocity was observed in the trench and rim cavity regions as would be expected because of the large turning of the flow in the main gas path by the vane. The isentropic exit Mach number for the vane in the main gas path is shown in Fig. 7 as a reference.

Figure 7 shows the Mach numbers in the trench and rim cavity, which were calculated according to the isentropic flow equations from the ratio of the measured total to static pressures. The total and static pressures were measured using Kiel pressure probes and static pressure taps at discrete locations in the rim cavity and trench. The legend in Fig. 7 shows where the total pressures were measured for each location with Kiel pressure probes aligned with

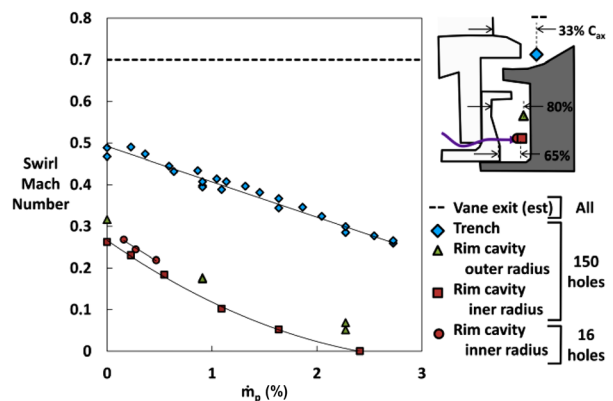


Fig. 7 Swirl Mach number in the trench region and the rim cavity for a range of purge flow rates

the circumferential direction. The measurements were made in the trench (33% axial chord downstream of the vane trailing edge and $r/b = 0.97$), at the rim cavity outer radius (80% of the rim cavity axial width and $r/b = 0.92$), and at the rim cavity inner radius (65% of the rim cavity axial width and $r/b = 0.90$). The Kiel pressure probes were insensitive to flow angle deviations of ± 30 deg. It is important to note that the flow in the trench and in the rim cavity was almost exclusively in the tangential, or swirl, direction, so Fig. 7 shows the Mach number for the flow in the swirl direction.

The measured Mach number variation in the trench and rim cavity is shown in Fig. 7 for a range of purge flow rates for the previously mentioned flow geometries: 16 and 150 purge holes. Figure 7 shows that significant swirl velocities were measured in the trench area and, although lower in magnitude but comparable to the vane exit Mach number, there were significant swirl velocities in the rim cavity. Since there was no rotor present in these experiments, the swirl in the trench was induced by shear from the flow exiting the vane in the main gas path. The high swirl velocities in Fig. 7 are important to keep in mind as one considers the sealing effectiveness of the purge flow since the purge flow entered as discrete jets in a relatively strong crossflow. Within the rim cavity, the swirl Mach number appeared to be insensitive to the number of holes indicating that for a given purge flow, the swirl flow in the rim cavity was found to be consistent no matter whether the purge flow was issued from 16 holes or 150 holes, further suggesting that the swirl flow was due to the shear from the vane exit flow.

As expected, the swirl decreased with decreasing radius: the trench swirl Mach number was lower than that of the vane exit, and the rim cavity swirl Mach number was lower than that of the trench. The swirl Mach number decreased with increasing purge flow in the trench and in the rim cavity. As the purge flow increased, ingestion decreased, which resulted in lower swirl velocities propagating into the rim cavity from the main gas path. This behavior was slightly exaggerated compared to a rim cavity with a rotor, since the swirl in a rotating rim cavity would not go to zero as shown in Fig. 7.

Sealing Effectiveness With Purge Flow

As was stated previously, the focus of this paper was to investigate the sealing effectiveness as a function of the purge flow delivery method into the rim cavity. Two configurations of purge flow delivery were used: Case 1: 150 purge holes and case 2: 16 purge holes. In both cases, the mate face gaps were sealed, and the turbine was operated at the design flow conditions as shown in Fig. 5.

Case 1: 150 Purge Holes. The first flow configuration presented in this paper is for 150 purge holes equally spaced around the circumference. The intent of using 150 holes, relative to the case with only 16 purge holes, was to uniformly distribute the purge flow in the rim cavity. The concentration effectiveness, as previously defined, is presented in Fig. 8 for both the stator and rotor sides of the rim cavity at the purge hole radius for the 150 purge hole configuration. The inset image shows the locations of the purge holes as well as the measurement locations at the same radius as the purge holes.

The flow was uniform with circumferential position as shown in Fig. 8 for several purge flow rates. The standard deviation of all the measurements at a given purge flow rate and radial location was calculated, and circumferential uniformity was within an average standard deviation of $\epsilon_c = \pm 0.011$, and a maximum deviation of $\epsilon_c = \pm 0.018$, indicating the purge flow did indeed enter the rim cavity uniformly around the annulus. The data in Fig. 8 indicated that the effectiveness on the stator side was higher than the rotor side for $\dot{m}_p \leq 1.26\%$ at all the circumferential locations. For $\dot{m}_p > 1.7\%$, however, the rotor side effectiveness was higher than the stator side as will be discussed further later in the text.

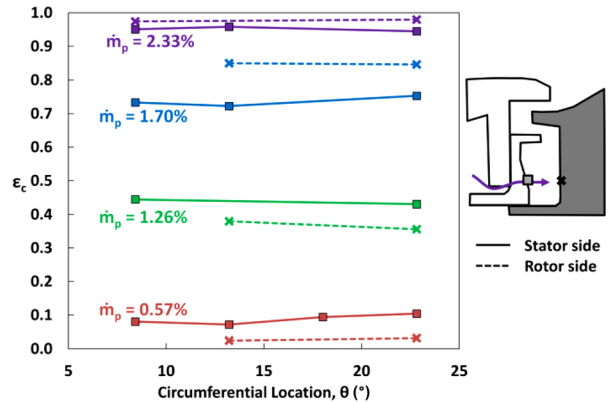


Fig. 8 Circumferential uniformity of concentration effectiveness for 150 purge holes for multiple purge flows

The concentration effectiveness is presented in Fig. 9 for a range of purge flow rates for the 150 purge hole configuration for different locations in the rim seal and cavity. The inset image shows the locations of the purge jets as well as the measurement locations. Wall static taps were used for the measurements as well as a sampling probe placed in the cavity. Figure 9 also shows schematics indicating the likely flow patterns in the rim seal and rim cavity for high and low purge flows as determined by the concentration effectiveness measurements.

As shown in Fig. 9, the concentration effectiveness increased with purge flow rate at all the locations as would be expected. Also, as expected, the highest concentration effectiveness values were at the locations deepest inside the cavity. At the low purge flows, the data in Fig. 9 indicated that the ingested flow was present throughout the rim seal and deep into the rim cavity. As the purge flow rate increased, the concentration effectiveness levels began to increase more prominently in the rim cavity relative to the rim seal. It was not until $\dot{m}_p = 1\%$ that the effectiveness on the stator and rotor sides of the rim seal began to increase indicating that at this purge flow rate, the walls of the rim seal were positively affected by the purge air. Although not shown here, effectiveness measurements were obtained in the rim seal axial gap between the stator and rotor sides. At low purge flows, effectiveness levels of $0.05 < \epsilon_c < 0.15$ were measured in the center of the axial gap identifying the path of the purge flow through the rim seal.

The concentration effectiveness measurements in Fig. 9 also indicated that the highest values for the sampling location were in the center of the cavity as compared to the stator and rotor walls for all the flow rates. These maximum concentration effectiveness levels indicated that most of the purge flow resided in the core of the rim cavity crossflow.

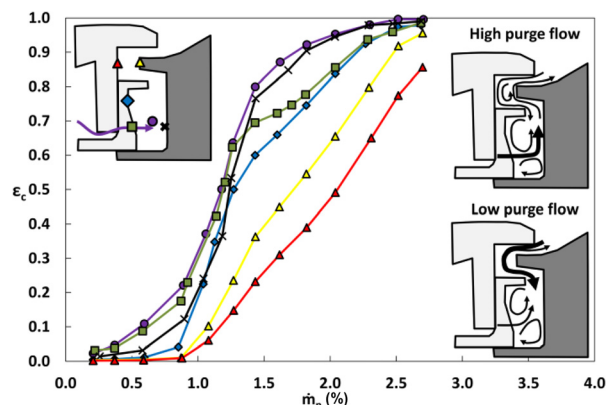


Fig. 9 Concentration effectiveness for 150 purge holes

The concentration effectiveness at the same radial location as the purge holes on the stator and rotor sides of the rim cavity exhibited different trends as shown in Fig. 9. A cross-over of the maximum effectiveness occurred at $\dot{m}_p = 1.35\%$. For $\dot{m}_p < 1.35\%$, the stator side of the rim cavity exhibited higher effectiveness than the rotor side. In contrast for $\dot{m}_p > 1.35\%$, the rotor side of the rim cavity exhibited higher effectiveness than the stator side. Figure 7 shows that there were high levels of swirl velocity at purge flow rates below 1.5%, which convected the purge flow in the swirl direction. As illustrated in Fig. 9, at low purge flows the jets entered the cavity with low momentum and did not penetrate far into the cavity and thereby did not reach the rotor cavity wall. Conversely at high purge flows, the jets entered the rim cavity with high momentum, which carried purge air to the rotor side of the cavity. The difference in purge jet trajectory is illustrated in the flow schematic images in Fig. 9 for the high purge flow and low purge flow cases. Since the swirl velocity in the cavity was a confined crossflow, the effectiveness on the stator side increased monotonically with purge flow rate; however, as the purge flow entered into the cavity crossflow, the rate of increase in effectiveness with flow rate was lower for the stator side of the rim cavity than the other locations between $1.5\% < \dot{m}_{\text{purge}} < 2.5\%$.

On the stator side of the rim cavity outboard of the purge holes, the effectiveness trend was similar to that of the stator side at the purge hole radius but at lower effectiveness values, as shown in Fig. 9. These results were consistent with the fact that some of the purge flow mixed with the rim cavity core flow before exiting the cavity. The flow schematic images show that as the purge flow entered the rim cavity, the flow likely induced a counter-clockwise rotating circulation in the rim cavity outboard of the purge holes. The flow recirculation region likely existed at this location inboard of the rim seal inner clearance, which caused the ingested flow to recirculate as shown in the flow schematic images in Fig. 9, similar to behavior shown by previous rim seal studies [2,3,8].

The concentration effectiveness was higher in the cavity than in the rim seal as shown in Fig. 9. For example, at $\dot{m}_p = 1.5\%$, the average effectiveness in the rim cavity was 0.75 while effectiveness was only 0.3 in the rim seal. In the rim seal, the effectiveness was higher on the rotor side than on the stator side, indicating the purge flow entered the rim seal from the rim cavity and convected along the rotor side of the rim seal. In contrast to the purge flow, the ingested flow mainly stayed on the stator side of the rim seal. This type of flow pattern is typical of a rim cavity with a rotor due to disk pumping and the thermal buffering effect [19,20], however, it is interesting to note a consistent trend in this static rim seal where rotational effects have been removed.

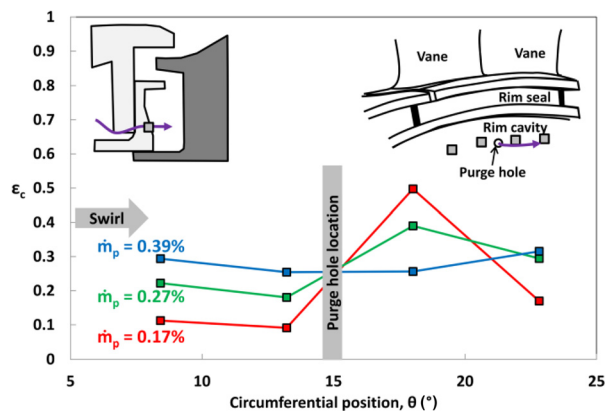


Fig. 10 Circumferential variation of concentration effectiveness for 16 purge holes on the stator side of the rim cavity at the purge hole radius for multiple purge flows

Case 2: 16 Purge Holes. The second configuration for introducing the purge flow was the case with only 16 uniformly distributed purge holes around the circumference. The intent of using 16 holes was to understand the importance of the number of holes where discrete jets were used to locally provide purge flow to the rim cavity. The purge holes used in this configuration were the same diameter as the 150 holes and were located at the same radius. As such, the momentum of each jet for the 16 holes was significantly higher than for the case with 150 holes for a given purge flow rate.

With 16 purge holes around the circumference of the rim cavity, concentration effectiveness was expected to vary with circumferential position. The circumferential variation of the concentration effectiveness on the stator side of the rim cavity at the purge hole radius is shown in Fig. 10 for three purge flow rates. The inset images in Fig. 10 show the measurement locations in the rim cavity as well as the purge hole location at $\theta = 15$ deg. Note the swirl direction as induced from the vanes was clockwise in the inset image. Concentration effectiveness is only shown for the stator side of the cavity as limited data were acquired for the rotor side.

Significant circumferential variation in concentration effectiveness can be seen in Fig. 10, especially at low purge flows. The purge jets behaved like a jet-in-crossflow with a decay in effectiveness with increasing circumferential distance from the purge hole. At low purge flows, the jets entered the cavity with low momentum and convected mainly along the stator side. At $\dot{m}_p = 0.17\%$, the effectiveness increased sharply downstream of the purge hole. At $\dot{m}_p = 0.27\%$, the same trend was observed as with $\dot{m}_p = 0.17\%$ with increased effectiveness downstream of the jet injection, but lower concentration effectiveness than at the $\dot{m}_p = 0.17\%$ indicating that the purge jet separated from the stator wall. At the highest purge flow rate of $\dot{m}_p = 0.39\%$, the concentration effectiveness was mostly uniform with circumferential direction on the stator side, indicating that the purge jet was completely separated from the stator wall.

Figure 11 shows the variation in concentration effectiveness with purge flow rate for the four sampling locations on the rim cavity stator side. The inset images show the measurement locations in the rim cavity, with the different circumferential locations as indicated in the figure. Similar to Figs. 10 and 11, there was significant circumferential variation in concentration effectiveness, especially from $0.15\% < \dot{m}_p < 0.4\%$. The effectiveness increased downstream of the purge hole, then decayed as the distance from the purge hole increased, particularly for $\dot{m}_p < 0.3\%$ where the effectiveness at $\theta = 18$ deg was significantly higher than at other circumferential locations.

The effectiveness at $\theta = 18$ deg behaved similar to that of a jet-in-crossflow. As shown in Fig. 7, significant swirl velocities are

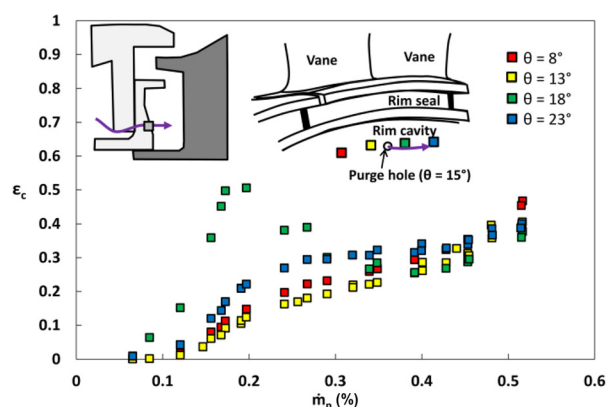


Fig. 11 Variation of concentration effectiveness with purge flow rate on the stator side of the rim cavity at the purge hole radius for 16 purge holes

measured in the cavity for 16 purge holes. The concentration effectiveness shown in Fig. 11 increased sharply with increasing purge flow rate where the jet appeared to remain attached to the stator wall up to $\dot{m}_p = 0.2\%$. As the purge flow increased, the jet momentum increased such that the purge flow separated from the stator wall, and the effectiveness gradually decayed with flow rate up to $\dot{m}_p = 0.4\%$. The effectiveness at the remaining sampling locations increased monotonically with purge flow rate, although the rate of increase in effectiveness decreased for $\dot{m}_p > 0.2\%$, where the jet appeared to separate from the stator side of the cavity. The jet did not appear to reattach to the stator wall for $\dot{m}_p > 0.35\%$, but the effectiveness for $\theta = 23$ deg exhibited higher effectiveness for $0.35\% < \dot{m}_p < 0.5\%$, indicating the purge flow jet mixed with the cavity cross flow as it swirled around the rim cavity.

The variation in effectiveness with purge flow rate at the four circumferential locations was averaged in Fig. 12 for each location indicated in the inset image. As observed in Fig. 11, effectiveness increased with purge flow rate for $\dot{m}_p < 0.2\%$, beyond which the rate of increase in effectiveness decreased up to $\dot{m}_p = 0.4\%$. The momentum of the purge flow caused the jets to penetrate farther into the rim cavity where the flow mixed with the ingested swirl flow. Limited concentration effectiveness measurements were averaged for the rotor side and are shown in Fig. 12. The concentration effectiveness in Fig. 12 indicated that the purge flow penetrated farther into the rim cavity at high purge flow rates, which is consistent with high momentum jets. The cross-over point where the rotor side effectiveness was higher than the stator side effectiveness occurred at $\dot{m}_p = 0.4\%$ for 16 purge holes. Recall that for 150 purge holes, a similar cross-over occurred at $\dot{m}_p = 1.35\%$ as shown in Fig. 9.

The stator side of the rim seal showed zero effectiveness over the range of flow rates, as shown in Fig. 12. This trend was similar to Fig. 9, which showed zero effectiveness for $\dot{m}_p < 1\%$ in the rim seal. The data showed that significant ingestion occurred in the rim seal for 16 purge holes. At the outer radius on the stator side of the cavity, the effectiveness was again seen in Fig. 12 to be lower than at the purge hole radius, which was similar to Fig. 9 for 150 purge holes. The reduced effectiveness inboard of the rim seal on the stator side was evidence of the flow recirculation for 16 purge holes similar to 150 purge holes, as shown in Fig. 9.

Sealing Effectiveness With Mate Face Gap Leakage Flow

The focus of this section is on the sealing effectiveness for different methods of introducing purge and leakage flows into the rim seal and rim cavity, specifically the mate face gap leakage that flowed through the gaps between adjoining vane doublets into the rim seal. For the effectiveness measurements presented in this

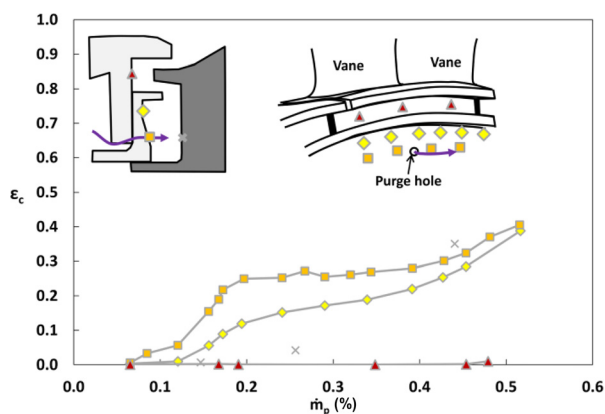


Fig. 12 Averaged concentration effectiveness for 16 purge holes

section, as was previously mentioned, two configurations of mate face gap leakage flow were used: Case 3: mate face gap leakage only, and case 4: mate face gap leakage with 16 purge holes. Again the vane was operated at aerodynamic design conditions as previously discussed.

Case 3: MFG Leakage Flow Only. For the mate face gap studies reported for case 3, there was no purge flow present. The purpose of this configuration was to identify any contributions of the mate face gap leakage flow on the concentration effectiveness in the rim seal and the rim cavity. Concentration effectiveness for the mate face gap leakage case is given in Fig. 13. Note that the maximum flow was lower than the purge flows, which is consistent with what would occur in an operating turbine. The inset images show the vane doublet, the rim seal, and the mate face gap leakage slots located at 0% and 100% pitch in the circumferential direction. Note that the swirl direction was clockwise. Three sampling taps were distributed circumferentially through the stator side of the rim seal as shown in the inset image, and three sampling taps were located on the stator side of the rim cavity.

There was a significant variation in the concentration effectiveness in the rim seal with mate face gap leakage flow rate and circumferential location as shown in Fig. 13. The concentration effectiveness increased with the mate face gap leakage flow at all the three sampling locations in the rim seal. The effectiveness was highest just downstream of the mate face gap leakage slot, as evidenced by the measurements at 15% pitch, followed by a decay in effectiveness with increasing distance from the slot, as shown by the measurements at 40% and 65% pitch. The mate face gap leakage flow was similar to an angled planar jet in a strong cross flow, with the highest effectiveness just downstream of the flow injection location, followed by a decrease in effectiveness as the distance from the leakage slot increased.

The concentration effectiveness on the stator side of the rim cavity is also shown for the mate face gap leakage flow in Fig. 13. The concentration effectiveness increased with leakage flow rate, but never exceeded $\epsilon_c = 0.2$. The effectiveness was observed to be uniform in the cavity for a given mate face gap leakage flow rate, so Fig. 13 only shows one symbol at each flow rate. The uniform effectiveness for a given flow rate suggested that the mate face gap leakage mixed with the ingested main gas path flow and entered the rim cavity with uniform concentration regardless of circumferential location. Thus, the mate face gap leakage contributed to the sealing effectiveness in the rim cavity and was shown to be circumferentially uniform.

Case 4: MFG With 16 Purge Holes. The fourth case is for the mate face gap leakage with 16 purge holes. The purpose of this configuration was to determine the sensitivity of the 16 purge holes to the mate face gap leakage flow. This configuration was a

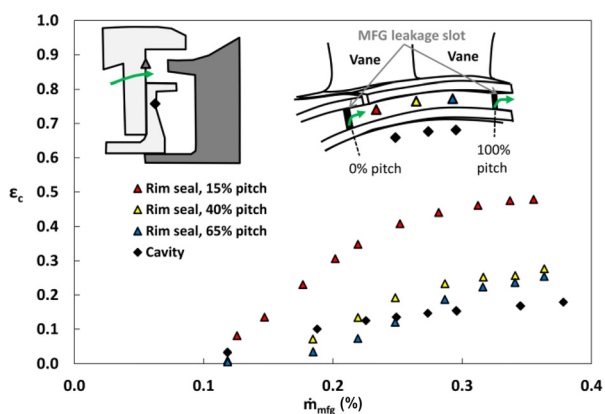


Fig. 13 Concentration effectiveness for mate face gap leakage flow only (no purge)

combination of case 2: 16 purge holes and case 3: mate face gap leakage only.

The circumferential variation of concentration effectiveness is presented in Fig. 14 for both the stator and rotor sides of the rim cavity (solid and dashed lines, respectively) at the purge hole radius for three flow rates. As in previous figures, the inset image shows the measurement locations, and the purge hole location is shown in the graph at $\theta = 15$ deg. It should be noted that the flow rates presented in the figure are the sum of the purge and mate face gap leakage flow rates.

Concentration effectiveness increased with purge and leakage flow rate in Fig. 14. The results were similar to those for 16 purge holes as shown in Fig. 10 with significant circumferential variation in effectiveness. At $\dot{m}_p + \dot{m}_{mfg} = 0.48\%$, the concentration effectiveness on the stator side of the rim cavity showed an increase at $\theta = 18$ deg similar to that seen at low purge flow rates in Fig. 10. The effectiveness on the rotor side was essentially constant for 0.48% indicating the purge flow stayed attached to the stator side of the cavity and convected to the rotor side of the cavity only through mixing with the rim cavity swirl flow. At a slightly higher flow rate of $\dot{m}_p + \dot{m}_{mfg} = 0.77\%$, the stator side effectiveness was mostly uniform, and the rotor side of the cavity exhibited a local maximum in concentration effectiveness at $\theta = 18$ deg, indicating the higher momentum of the purge flow jet carried high concentration purge air to the rotor side of the cavity. The effectiveness on the rotor side decreased with distance downstream of the purge hole location. At an even higher flow rate of $\dot{m}_p + \dot{m}_{mfg} = 0.95\%$, the trend was even more pronounced, with the maximum concentration effectiveness again at $\theta = 18$ deg on the rotor side. At this highest flow condition, the high momentum of the purge jets resulted in a local concentration effectiveness maximum on the rotor side of the cavity across from the purge holes, again followed by a decrease with distance from the purge jets.

Scaling of Sealing Effectiveness for Purge

This section presents a comparison of the different purge flow configurations tested in the rim cavity for case 1: 150 purge holes and case 2: 16 purge holes. The mate face gap leakage was shown to affect concentration effectiveness locally in the rim seal, but showed little effect in the rim cavity so the mate face gap leakage will not be used in this comparison.

The concentration effectiveness for both 150 purge holes and 16 purge holes is presented in Fig. 15 for the range of purge flow rates shown previously. The two inset images contain corresponding legends for each configuration indicating each measurement location in the rim cavity, as shown in Figs. 9 and 12. Note that since the diameter of the holes was the same for both cases, the

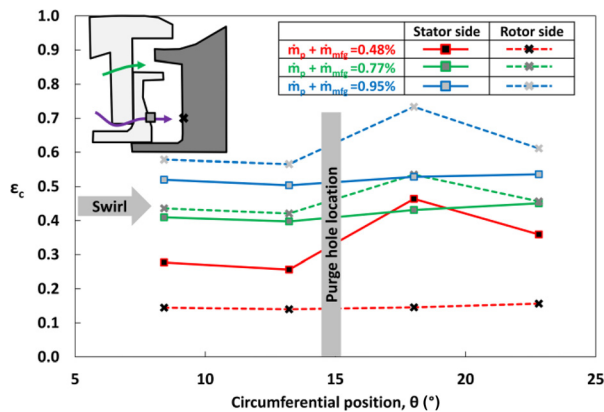


Fig. 14 Circumferential variation in concentration effectiveness on the stator and rotor sides of the rim cavity for 16 purge holes and the mate face gap leakage

range of tested flow rates was smaller for 16 purge holes than 150 holes. Of primary interest in Fig. 15 was that concentration effectiveness was higher for 16 purge holes than for 150 purge holes at a given flow rate. The trend of higher concentration effectiveness for 16 purge holes compared to 150 purge holes was observed at all the sampling locations in the rim cavity.

It is clear from the measurements shown in this paper that the dynamics of the purge jet affect the concentration effectiveness throughout the rim cavity. Similar to a film cooling jet issued into a crossflow, the purge jets can also be evaluated in terms of two physical parameters that govern jet dynamics, namely, the mass flux (blowing) ratio, M , and the momentum flux ratio, I . It is worth noting that the density ratio, $DR = \rho_p / \rho_{rc}$, was approximately 1.1 for the experiments presented in this paper. The crossflow velocity used in the definitions of the mass and momentum flux ratios was calculated from the swirl Mach number presented in Fig. 7.

The two purge flow configurations had notably different mass flux and momentum flux ratios for a given purge flow. Figure 16 shows the mass and momentum flux ratios for a range of purge flow rates for both 150 purge holes and 16 purge holes. The mass and momentum flux ratios of the 16 purge holes were approximately an order of magnitude higher than that of the 150 purge holes for a given flow rate.

Recall that there was a cross-over in concentration effectiveness between the rotor side of the rim cavity and the stator side as shown in Figs. 9 and 12. At low purge flow rates, the stator side exhibited higher effectiveness, and at higher purge flow rates, the rotor side was higher. The cross-over flow rate for 150 purge holes is shown in Fig. 9 to be $\dot{m}_p = 1.35\%$. This corresponded to a mass flux ratio of $M = 2.7$ and a momentum flux ratio of 6.5 in Fig. 16. The cross-over flow rate for the 16 purge holes shown in Fig. 12 is approximately $\dot{m}_p = 0.4\%$, which corresponded to $M = 2.6$ and $I = 6$ in Fig. 16. The consistency between the cross-over point in both purge flow configurations indicated that similar jet dynamics resulted in similar effectiveness trends in the rim cavity. The agreement also suggested that it was reasonable to scale the effectiveness measurements with M and I .

The concentration effectiveness in the rim cavity for both 150 purge holes and 16 purge hole is shown as a function of the mass flux ratio in Fig. 17 and as a function of momentum flux ratio in Fig. 18. It should be noted that since the rim cavity swirl velocity approached zero as the purge flow increased, M and I lose meaning, so the data are only shown up to $M = 10$ and $I = 25$.

Figure 17 shows that the concentration effectiveness measurements nearly collapsed for 150 purge holes and 16 purge holes for $M < 1.2$. The concentration effectiveness levels at the purge hole radius on the stator side agreed up to the point where the effectiveness of the 16 purge holes began to level off, suggesting that insufficient flow was provided to fully purge the cavity with only 16 purge holes. Overall mass flow rate is important to fully seal

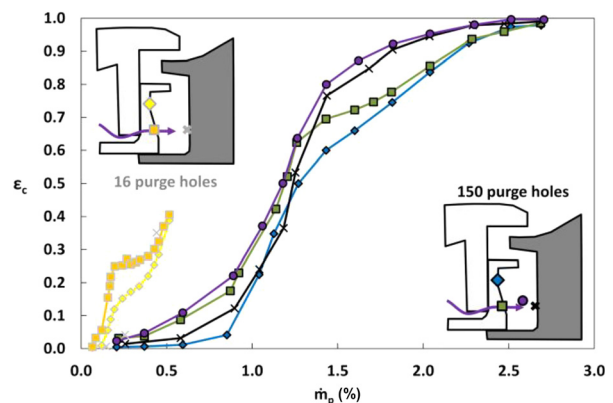


Fig. 15 Concentration effectiveness for 150 purge holes and 16 purge holes with varying purge flow rates

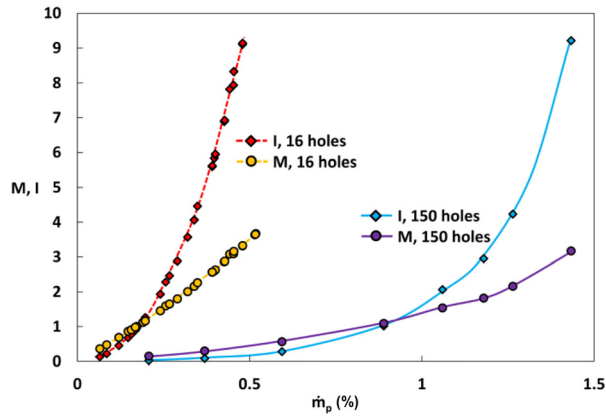


Fig. 16 Mass flux ratio, M , and momentum flux ratio, I , for 150 purge holes and 16 purge holes

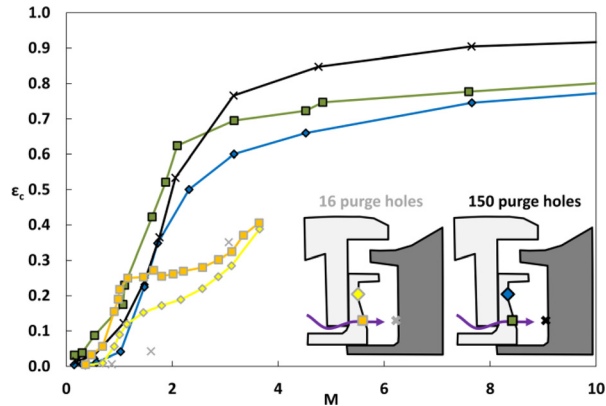


Fig. 17 Concentration effectiveness for 150 purge holes and 16 purge holes plotted against blowing ratio

cavities and an intermediate number of purge holes may provide sufficient mass flow rate and jet momentum to fully purge the cavity. The effectiveness on the rotor side of the rim cavity was much lower for 16 holes than for 150 holes, but the cross-over point discussed previously was seen to be consistent for both cases at $M = 2.6$.

In Fig. 18, the concentration effectiveness measurements also collapsed for 150 purge holes and 16 purge holes for $I < 1.3$. Again, the concentration effectiveness measurements on the stator side of the rim cavity exhibited similar values for both 150 and 16 purge holes up to $I = 1.3$, where the concentration effectiveness

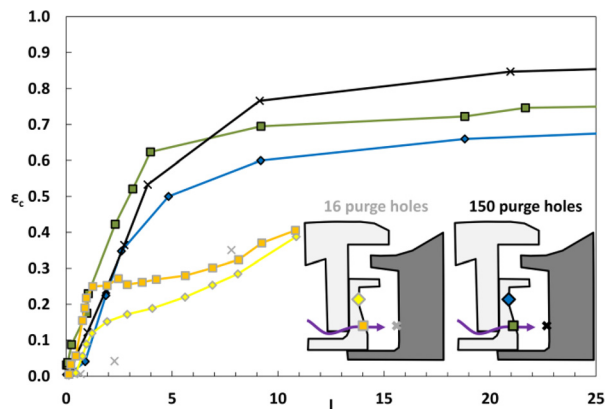


Fig. 18 Concentration effectiveness for 150 purge holes and 16 purge holes plotted against momentum flux ratio

leveled off for 16 purge holes. The cross-over point where the rotor side effectiveness was higher than the stator side effectiveness was shown for both cases at $I = 6$. Additional purge hole configurations between 16 and 150 may provide scaling across a wider range of mass flux and momentum flux ratios.

Conclusion

The sealing of rim cavities is very important for gas turbine engines in order to avoid catastrophic failures resulting from hot gas ingestion between stages and other gaps. The results presented in this paper for a static vane with engine-relevant hardware operated at design conditions indicated the importance of understanding the usage of secondary air supplies. Sealing effectiveness levels for different methods of introducing purge and leakage flow into the rim seal and rim cavity were presented. The sealing effectiveness results were presented for four different configurations to investigate the number of purge holes as well as the influence of the mate face gap leakage.

High swirl velocities were measured in the trench region, which were important for understanding how the jets from the purge flow reacted in the rim cavity. The purge jets were found to be similar to that of a jet-in-crossflow while the mate face gap leakage was similar to that of a planar jet-in-crossflow.

The sealing effectiveness was highly dependent upon how the purge flow was introduced into the cavity. The results indicated better sealing with fewer purge holes as opposed to a large number of holes. Fewer purge holes resulted in higher momentum flux jets for a given purge flow rate as compared to a larger number of holes. No matter the number of purge holes, the concentration effectiveness exhibited a cross-over in the maximum sealing effectiveness at the same mass flux ratio and momentum flux ratio. For low jet momentum flux ratios, the sealing effectiveness on the stator side was higher than on the rotor side of the rim cavity, while for high jet momentum flux ratios, the sealing effectiveness on the rotor side was higher than the stator side of the cavity. It should be noted that when a rotor is included in future studies, the disk pumping may decrease the value of M and I corresponding to the cross-over point.

The mate face gap leakage flow affected sealing effectiveness in the circumferential direction in the rim seal. Uniform sealing effectiveness was measured in the rim cavity as the mate face gap leakage mixed with the ingested flow before entering the rim cavity. As such, the mate face gap leakage flow contributed a small amount to the sealing effectiveness in the rim cavity.

The results from these initial studies have indicated the complexity of the flow field in the rim seal and cavity and the importance of understanding the flows for determining better sealing methods. Because of the flow field complexity, there is a need for high fidelity predictive methods to accurately model the seal air and cavity flow physics to predict sealing effectiveness. These experiments at engine-relevant conditions will help validate new designs and computational tools. Future studies will include rotational effects in the full 1.5-stage turbine, which may further complicate the flow field in the rim seal and cavity.

Acknowledgment

The authors would like to thank Pratt & Whitney and the Department of Energy National Energy Technologies Laboratory for sponsoring the research presented in this paper.

Nomenclature

- b = hub radius
- c = gas concentration
- C_x = axial chord length
- h = height
- I = momentum flux ratio ($\rho_p V_p^2 / (\rho_{rc} V_{rc}^2)$)
- M = mass flux (blowing) ratio ($\rho_p V_p / (\rho_{rc} V_{rc})$)

\dot{m}_{mfg} = MFG leakage flow based on full span turbine flow rate
 \dot{m}_{purge} = purge flow based on full span turbine flow rate
 $\dot{m}_{\text{sec,air}}$ = secondary air supply mass flow rate
 p, p_t = static and total pressure
 r = radius
 Re_x = vane exit axial Reynolds number
 s = spacing
 s_c = seal clearance
 S/S_{max} = percent wetted surface distance
 V = velocity
 x = axial direction
 $\Delta p/p_{t,\text{in}}$ = nondimensional pressure difference $((p_{\text{max}} - p_{\text{min}})/p_{t,\text{in}})$
 ϵ_c = concentration effectiveness $((c - c_{\infty})/(c_s - c_{\infty}))$
 θ = circumferential direction
 μ = dynamic viscosity
 ρ = fluid density

Subscripts and Abbreviations

in = turbine inlet parameter
 mfg = mate face gap
 p = purge
 rc = rim cavity
 rs = rim seal
 s = secondary flow supply parameter
 TE = trailing edge
 1VP = first vane plenum
 ∞ = main gas path parameter

References

- [1] Abe, T., Kikuchi, J., and Takeuchi, H., 1979, "An Investigation of Turbine Disk Cooling (Experimental Investigation and Observation of Hot Gas Flow Into a Wheel-space)," 13th International Congress on Combustion Engines (CIMAC), Vienna, Austria, May 7–10, Paper No. GT30.
- [2] Sangan, C. M., Pountney, O. J., Zhou, K., Wilson, M., Michael Owen, J., and Lock, G. D., 2012, "Experimental Measurements of Ingestion Through Turbine Rim Seals—Part I: Externally Induced Ingress," *ASME J. Turbomach.*, **135**(2), p. 021012.
- [3] Phadke, U. P., and Owen, J. M., 1988, "Aerodynamic Aspects of the Sealing of Gas-Turbine Rotor-Stator Systems—Part I: The Behavior of Simple Shrouded Rotating-Disk Systems in a Quiescent Environment," *Int. J. Heat Fluid Flow*, **9**(2), pp. 98–105.
- [4] Sangan, C. M., Pountney, O. J., Zhou, K., Owen, J. M., Wilson, M., and Lock, G. D., 2012, "Experimental Measurements of Ingestion Through Turbine Rim Seals—Part II: Rotationally Induced Ingress," *ASME J. Turbomach.*, **135**(2), p. 021013.
- [5] Graber, D. J., Daniels, W. A., and Johnson, B. V., 1987, "Disk Pumping Test," Aero Propulsion Laboratory, Wright-Patterson Air Force Base, Dayton, OH, Report No. FWRL-TR-2050.
- [6] Johnson, B., Mack, G., Paolillo, R., and Daniels, W., 1994, "Turbine Rim Seal Gas Path Flow Ingestion Mechanisms," *AIAA Paper No. 1994-2703*.
- [7] Feiereisen, J. M., Paolillo, R. E., and Wagner, J., 2000, "UTRC Turbine Rim Seal Ingestion and Platform Cooling Experiments," *AIAA Paper No. 2000-3371*.
- [8] Gibson, J., Thole, K., Christophel, J., and Memory, C., 2015, "Effects of the Main Gas Path Pressure Field on Rim Seal Flows in a Stationary Linear Cascade," *ASME Paper No. GT2015-43517*.
- [9] Sangan, C. M., Pountney, O. J., Scobie, J. A., Wilson, M., Owen, J. M., and Lock, G. D., 2013, "Experimental Measurements of Ingestion Through Turbine Rim Seals—Part III: Single and Double Seals," *ASME J. Turbomach.*, **135**(5), p. 051011.
- [10] Scobie, J. A., Teuber, R., Li, Y. S., Sangan, C. M., Wilson, M., and Lock, G. D., 2016, "Design of an Improved Turbine Rim-Seal," *ASME J. Eng. Gas Turbines Power*, **138**(2), p. 022503.
- [11] Coren, D. D., Atkins, N. R., Long, C. A., Eastwood, D., Childs, P. R. N., Guijarro-Valencia, A., and Dixon, J. A., 2011, "The Influence of Turbine Stator Well Coolant Flow Rate and Passage Configuration on Cooling Effectiveness," *ASME Paper No. GT2011-46448*.
- [12] Andreini, A., Da Soghe, R., and Facchini, B., 2010, "Turbine Stator Well CFD Studies: Effects of Coolant Supply Geometry on Cavity Sealing Performance," *ASME J. Turbomach.*, **133**(2), p. 021008.
- [13] Teuber, R., Li, Y. S., Maltson, J., Wilson, M., Lock, G. D., and Owen, J. M., 2013, "Computational Extrapolation of Turbine Sealing Effectiveness From Test Rig to Engine Conditions," *Proc. Inst. Mech. Eng. Part J*, **227**(2), pp. 167–178.
- [14] Owen, J. M., 2010, "Prediction of Ingestion Through Turbine Rim Seals—Part II: Externally Induced and Combined Ingress," *ASME J. Turbomach.*, **133**(3), p. 031006.
- [15] Bunker, R. S., Laskowski, G. M., Bailey, J. C., Palafox, P., Kapetanovic, S., Itzel, G. M., Sullivan, M. A., and Farrell, T. R., 2011, "An Investigation of Turbine Wheel-space Cooling Flow Interactions With a Transonic Hot Gas Path—Part 1: Experimental Measurements," *ASME J. Turbomach.*, **133**(2), p. 021015.
- [16] Barringer, M., Coward, A., Clark, K., Thole, K., Schmitz, J., Wagner, J., Alvin, M. A., Burke, P., and Dennis, R., 2014, "Development of a Steady Aero Thermal Research Turbine (START) for Studying Secondary Flow Leakages and Airfoil Heat Transfer," *ASME Paper No. GT2014-25570*.
- [17] Clark, K., Barringer, M., Coward, A., Thole, K., Clum, C., Hiester, P., Memory, C., and Robak, C., 2016, "Using a Tracer Gas to Deduce Sealing Effectiveness for an Engine Realistic Rim Seal Geometry," *ASME Paper No. GT2016-58095*.
- [18] Zhou, D. W., Roy, R. P., Wang, C.-Z., and Glahn, J. A., 2011, "Main Gas Ingestion in a Turbine Stage for Three Rim Cavity Configurations," *ASME J. Turbomach.*, **133**(3), p. 031023.
- [19] Pountney, O. J., Sangan, C. M., Lock, G. D., and Owen, J. M., 2013, "Effect of Ingestion on Temperature of Turbine Disks," *ASME J. Turbomach.*, **135**(5), p. 051010.
- [20] Cho, G. H., Sangan, C. M., Owen, J. M., and Lock, G. D., 2015, "Effect of Ingress on Turbine Discs," *ASME Paper No. GT2015-43234*.